ARTICLE IN PRESS

Available online at www.sciencedirect.com
SCIENCE DIRECT®

Journal of Magnetic Resonance 173 (2005) 97–115

JMR Journal of Magnetic Resonance

www.elsevier.com/locate/jmr

The SIMRI project: a versatile and interactive MRI simulator

H. Benoit-Cattin[a,*], G. Collewet[b], B. Belaroussi[a], H. Saint-Jalmes[c], C. Odet[a]

[a] CREATIS, UMR CNRS #5515, U 630 Inserm, Université Claude Bernard Lyon 1, INSA Lyon, Bât. B. Pascal, 69621 Villeurbanne, France
[b] CEMAGREF/Food Processes Engineering Research Unit, 17 av de Cucillé, 35044 Rennes, France
[c] Laboratoire de Résonance Magnétique Nucléaire—Méthodologie et Instrumentation en Biophysique, UMR CNRS 5012, Université Claude Bernard Lyon 1—CPE Lyon, France

Received 6 April 2004; revised 10 September 2004

Abstract

This paper gives an overview of SIMRI, a new 3D MRI simulator based on the Bloch equation. This simulator proposes an efficient management of the T_2^* effect, and in a unique simulator integrates most of the simulation features that are offered in different simulators. It takes into account the main static field value and enables realistic simulations of the chemical shift artifact, including off-resonance phenomena. It also simulates the artifacts linked to the static field inhomogeneity like those induced by susceptibility variation within an object. It is implemented in the C language and the MRI sequence programming is done using high level C functions with a simple programming interface. To manage large simulations, the magnetization kernel is implemented in a parallelized way that enables simulation on PC grid architecture. Furthermore, this simulator includes a 1D interactive interface for pedagogic purpose illustrating the magnetization vector motion as well as the MRI contrasts.

Keywords: MRI simulation; Bloch equation; Artefacts; Field inhomogeneity; Software

1. Introduction

The simulation of magnetic resonance imaging (MRI) is an important counterpart to MRI acquisitions. Simulation is naturally suited to acquire understanding of the complex MR phenomena [1]. It is used as an educational tool in medical and technical environments [2,3]. MRI simulation enables the investigation of artifact causes and effects [4,5]. Also, MRI simulation may help the development and optimization of MR sequences [4].

With the increased interest in computer-aided MRI image analysis methods (segmentation, data fusion, quantization...), there is greater need for objective methods of algorithm evaluation. Validation of in vivo MRI studies is complicated by lack of reference data (gold standard) and the difficulty of constructing anatomical realistic physical phantoms. In this context, an MRI simulator provides an interesting assessment tool [6] as it generates 3D realistic images from medical virtual objects that are perfectly known.

The simulators previously developed use different approaches and thus differ in closeness to the reality, extent of applicability, and necessary computation effort.

The first category of simulators use proton density, T_1 and T_2 maps computed from a set of images acquired using different repetition and echo times. Using these maps and equations of the image intensity for different pulse sequences, new images are synthesized [7–10]. The simulator proposed in [11] is based on the same approach but provides more realistic images as it includes phenomena such as noise, tissue heterogeneity, correlation between T_1, T_2, and proton density, influence of the field strength on the relaxation times, partial volume effect, and spatial non-uniformity of the signal. How-

* Corresponding author. Fax: +33 472 436 312.
E-mail address: yougz@creatis.insa-lyon.fr (H. Benoit-Cattin).

1090-7807/$ - see front matter © 2004 Elsevier Inc. All rights reserved.
doi:10.1016/j.jmr.2004.09.027

ever, this approach does not closely simulate the whole process of MR images formation and thus is not able to simulate all the artifacts encountered in MR images such as chemical-shift, intra-voxel dephasing, imperfection of slice selection, Gibbs phenomenon, aliasing, non-linear gradients, B_0 inhomogeneity, and radio-frequency (RF) inhomogeneity and susceptibility artifacts.

A second category of simulators uses the *k*-space formalism. The inverse Fourier transform of the spin density image is computed to create the *k*-space amplitudes [12]. Then, amplitudes are corrected to simulate the pulse sequence and the relaxation phenomena as well as stimulated echoes, a motion or transverse magnetization that propagates through several periods. The same approach was used in [13,14] to simulate tagging. One drawback of this approach is that each tissue type must be treated separately making the simulation of non-uniform tissue characteristics difficult. Moreover, the use of the transformation of the spin density maps implies strict relationships between gradient strength, sampling frequency, and field of view (FOV), thus disenabling the simulation of non-linear gradients on inhomogeneous magnetic field.

A third approach, "hybrid," is proposed in [15]. Each tissue type is associated with a spin model (defined by T_1, T_2, T_2^*, and proton density) that simulates intra-voxel heterogeneity by replacing a spin by a distribution of spins having different frequencies. The NMR intensities of each spin model are computed using the signal equation or a discrete-event Bloch equation computation. Then, images are formed by weighing the tissue distribution for each voxel with the signal of each tissue. Lastly, noise and partial volume effects are introduced in the images. This approach is very interesting regarding the simulation of intra-voxel heterogeneities. Yet, the simulation of non-uniform tissue characteristics (i.e., different intra-voxel heterogeneities conducting to different T_2^*) would require the simulation of a large number of spin models. Moreover, as the simulators of the first category, the hybrid approach can not simulate the whole MR image formation process and consequently the associated artifacts like those linked to the coding gradients neither.

The fourth category of simulators is based on a discrete-event Bloch equation [16] resolution applied on a spin system [1,4,5,17–21]. This approach is the closest to reality and is not limited except by the assumptions of the Bloch equation (no diffusion) and by the computation time. Most of the phenomena encountered during the MR image formation can thus be simulated but one should take care of the number of isochromats used to describe the object. As underlined in [1,15], the use of high number of isochromats per voxel associated to a frequency distribution provides a frame to simulate the intra-voxel dephasing as well as the corresponding spin echoes. However, using insufficient frequency spacing of the isochromats leads to spurious spin echoes, and a too small number of isochromats leads to truncation artifact [15]. The number of isochromats required is also linked to the T_2 constant or to the acquisition bandwidth and reaches 400 [15]. Such a number is much too high as it multiplies the simulation time accordingly. That is why several authors proposed alternate solutions. In [5], a special scheme based on the separation of each magnetization vector in two parts is proposed. In [19], a random spacing of the object points is used to simulate the echo formation properly. In [18,20,21], a linear change of B_0 across the voxel during the application of the gradient is assumed. However, these approaches do not consider voxel isochromat distribution and consequently only simulate an echo in presence of a gradient. The simulator presented in this paper includes an original approach to simulate the intra-voxel dephasing and a specific signal management for spin echo simulations.

This paper proposes an overview of a new 3D MRI simulator named *SIMRI* that is based on the Bloch equation resolution. *SIMRI* includes an efficient T_2^* management simulating properly spin echoes. It takes into account the main static field value and accepts a 3D map of the main field inhomogeneities to simulate the main MRI artifacts (chemical shift, susceptibility artifact, ...). It enables 2D slice selection with different kinds of RF pulse. Also, a parallel implementation adapted to grid technology [22] was developed to overcome the problem of computation time and to achieve the performances required by the targeted applications. Moreover, the kernel used for simulation of 2D or 3D images is also accessible through a highly interactive graphic interface for a better understanding of the MRI contrast phenomena and the spin magnetization vector evolution.

Section 2 of the paper gives an overview of the simulator through the presentation of its main components, i.e., virtual object description, sequence implementation, magnetization computation kernel, RF pulse shaping, and T_2^* modeling. Section 3 introduces simulation results. 1D, 2D, and 3D results are given, including artifact simulations. We focus on the simulator implementation in Section 4 by introducing the sequence programming strategy, the interactive simulation tool and the distributed implementation.

2. Simulator overview

2.1. Simulator overview

The simulator overview is given in Fig. 1. From a 3D virtual object, the static field definition and an MRI sequence, the magnetization kernel computes a set of RF signals, i.e., the *k*-space. To simulate realistic images,

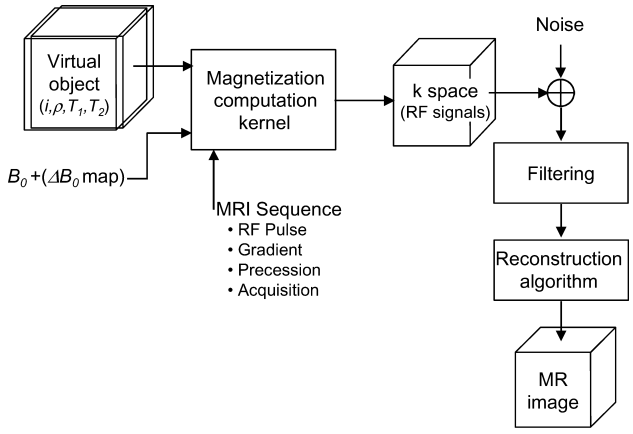

Fig. 1. SIMRI simulator overview.

noise can be added to the k-space that can be filtered (like in a real imager) before the reconstruction of the MR image (Modulus and phase) using fast Fourier transform (FFT) [23].

2.2. Virtual object description

The 3D virtual object is a discrete description of a real object spin system [23]. Each voxel of the virtual object contains a set of physical values that are necessary to compute the local spin magnetization vector with the Bloch equation. These values are the proton density (noted ρ) and the two relaxation constants T_1 and T_2. Basically, a virtual object describes the nuclear spin system of one component associated with the water proton. Note that *SIMRI* is able to deal with many components in order to simulate chemical shift artifact (see Section 3.6) or partial volume effect. Then, each voxel contains the ρ, T_1, and T_2 values of each component. The magnetization vector of each voxel is obtained by summation of the magnetization vector separately calculated for each component that is defined by its normalized resonance frequency. Such multi-component description enables the definition of realistic object [24]. It may also enable the correct simulation of multiple echoes when associating an isochromat frequency distribution to a set of components.

Then, a 3D virtual object of size $S = X \times Y \times Z$ voxels is described by $C \times S$ 3-tuple values, where C is the number of components modeling each object point. The object definition is completed by the object dimension and the normalized resonance frequency of each considered component.

2.3. Static field and field inhomogeneities

A local main field inhomogeneity ΔB is also associated with each virtual object voxel. We assume constant inhomogeneity within a voxel. The main field inhomogeneity is composed of two terms:

$$\Delta B(\vec{r})\vec{z} = \Delta B_s(\vec{r})\vec{z} + \Delta B_0(\vec{r})\vec{z}, \quad (1)$$

where $\vec{r} = (x, y, z)^{\mathrm{T}}$ is the spatial coordinate.

The first term $\Delta B_s(\vec{r})$ corresponds to the variation of the tissue susceptibility within the object. From the knowledge of the susceptibly value map, it can be efficiently computed before the MRI simulation by using boundary element methods [21] or boundary integral methods [25]. The second term $\Delta B_0(\vec{r})$ is not linked to the object property and defines the inhomogeneities of the main field itself. In real imager this term tends to be cancelled by shim coils.

Although we consider constant field inhomogeneity within a voxel, we want to be able to simulate T_2^* weighting that is induced by intra-voxel inhomogeneities. Thus, at each voxel, we define a value ΔB_i that represents the intra-voxel molecular inhomogeneities due to the presence within a voxel of numerous isochromats. We consider the case of a Lorenzian distribution of the isochromats frequencies. This leads to weighting the free induction decay (FID) signal by $e^{-\gamma \Delta B_i t}$ which is known as the T_2^* effect discussed in Section 2.6 and illustrated in Section 3.1. In such a case, T_2^*, T_2, and ΔB_i are linked by the following equation:

$$\frac{1}{T_2^*} = \frac{1}{T_2} + \gamma \Delta B_i. \quad (2)$$

Although the simulator works within the rotating frame defined by the main static field value B_0, B_0 is defined. Indeed, B_0 impacts the frequency offset of the different object components and as a consequence the chemical shift. It also scales the static field inhomogeneities in order to simulate intensity and geometric distortions correctly. These are function of the static field B_0.

Note that the static field definition and the virtual object are the main part of what we call an experiment. They are completed by the FOV definition, the object position within this FOV, the bandwidth of the receiver coil and the number of pixels of the MR image to be reconstructed.

2.4. MRI sequence

During an MRI experiment, the object is placed in the static magnetic field B_0 and is excited by electromagnetic events of two types: RF pulses referred to as B_1 field and magnetic field gradients. The excitation step is followed by the acquisition of the object magnetization state that is stored as a complex signal in the k-space [23]. The timing of the magnetic events with RF signal acquisitions defines the MRI sequence and determines how the k-space is filled and consequently also defines the final image characteristics.

In the *SIMRI* simulator we define four types of events that can be chained to build MRI sequences within a C language function (see Section 4.1). The first type

of events is a free precession just defined by its duration. The second one is a precession with application of gradients. It is specified by its duration and the gradient magnitudes in the three spatial directions. The third one is a 1D signal acquisition step along one direction. This requires the number of points to capture, the bandwidth, the readout gradient magnitude and the position of this signal in the k-space. The last type of events concerns the application of RF pulses. The first kind of RF pulse defined in *SIMRI* is a constant pulse specified by its duration, a flip angle and the rotation axis. Two other kinds of RF pulse (modeled by a sequence of constant pulses of equal duration) are also available: A sinc-shaped pulse and a user defined pulse. The sinc-shaped pulse is defined by its total duration, the number of lobes and the number of constant pulses used to simulate the sinc pulse. The user-defined pulse is described by a file where the number of constant pulses and the values of each constant pulse are defined. The total duration of the pulse and its rotation axis are specified by the user. Gradient values to be applied during the pulse can also be specified.

So far, RF inhomogeneity and gradient non linearity are not simulated but the chosen implementation allows one to include these sources of artifacts in the simulator.

2.5. Magnetization kernel

The magnetization computation kernel called during the simulation of an MRI sequence is based on the solutions of the 3D Bloch equation [16] giving the time evolution of the spin magnetization vector $\vec{M} = (M_x, M_y, M_z)^{\mathrm{T}}$ by:

$$\frac{\mathrm{d}\vec{M}}{\mathrm{d}t} = \gamma(\vec{M} \times \vec{B}) - \begin{pmatrix} M_x/T_2 \\ M_y/T_2 \\ (M_z - M_0)/T_1 \end{pmatrix}, \tag{3}$$

where M_0 is the spin magnetization equilibrium value depending on the proton density ρ, (T_1, T_2) are the relaxation constants and γ is the gyromagnetic constant of the considered component (42.58 MHz/T for the water proton). The local magnetic field $\vec{B}$ is modeled as follows:

$$\vec{B}(\vec{r}, t) = B_0\vec{z} + \Delta B(\vec{r})\vec{z} + (\vec{G}(t)\vec{r})\vec{z} + \vec{B}_1(t), \tag{4}$$

where B_0 is the main static magnetic field, $\Delta B(\vec{r})$ is the local field inhomogeneities defined in Eq. (1), $\vec{G}(t)$ is the applied field gradient, $\vec{B}_1(t)$ is the RF pulse and $\vec{r} = (x, y, z)^{\mathrm{T}}$ is the spatial coordinate.

The simulation kernel implements a discrete time solution [17] of the Bloch equation by the means of rotation matrices and exponential scaling depending on the magnetic events of the MRI sequence. The magnetization vector evolution is iteratively computed according to the following equation:

$$\vec{M}(\vec{r}, t + \Delta t) = Rot_z(\theta_g)\, Rot_z(\theta_i)\, R_{\mathrm{relax}}\, R_{\mathrm{RF}} \vec{M}(\vec{r}, t), \tag{5}$$

where $Rot_z(\theta)$ is a rotation matrix about the z axis associated to the angle θ by:

$$Rot_z(\theta) = \begin{pmatrix} \cos\theta & \sin\theta & 0 \\ -\sin\theta & \cos\theta & 0 \\ 0 & 0 & 1 \end{pmatrix}, \tag{6}$$

where θ_g is linked to the applied gradient $\vec{G}(t)$ by:

$$\theta_g = \gamma\vec{r} \int_t^{t+\Delta t} \vec{G}(\tau)\,\mathrm{d}\tau, \tag{7}$$

where θ_i is linked to the field inhomogeneities by:

$$\theta_i = \gamma\,\Delta B(\vec{r})\,\Delta t, \tag{8}$$

where R_{relax} describes the relaxation effects by:

$$R_{\mathrm{relax}} = \begin{pmatrix} \mathrm{e}^{-\frac{\Delta t}{T_2(\vec{r})}} & 0 & 0 \\ 0 & \mathrm{e}^{-\frac{\Delta t}{T_2(\vec{r})}} & 0 \\ 0 & 0 & 1 - \mathrm{e}^{-\frac{\Delta t}{T_1(\vec{r})}} \end{pmatrix}, \tag{9}$$

and where R_{RF} represents the rotating effect of an RF pulse of phase angle ϕ leading to a flip angle α in a time Δt. When no gradient is applied during the pulse and when only one component on resonance is considered, R_{RF} is given (Eq. (10)) by a combination of rotating matrixes about z and x axis [23]:

$$R_{\mathrm{RF}} = Rot_z(\phi)\, Rot_x(\alpha)\, Rot_z(-\phi). \tag{10}$$

When the local experienced field is different from B_0, an effective flip angle α' is obtained locally in each voxel and the R_{RF} operator takes the general form given by Eq. (11).

$$R_{\mathrm{RF}} = Rot_z(\phi)\, Rot_y(\beta)\, Rot_x(\alpha')\, Rot_y(-\beta)\, Rot_z(-\phi), \tag{11}$$

where the effective flip angle α' is given by:

$$\alpha' = -\Delta t\sqrt{(\Delta\omega)^2 + \left(\frac{\alpha}{\tau}\right)^2} \tag{12}$$

and

$$\beta = \tan^{-1}\left(\frac{\Delta\omega}{\alpha/\Delta t}\right), \tag{13}$$

where $\Delta\omega$ is local value of the frequency offset $\Delta\omega(\vec{r}, t)$ which is linked to the local field value (Eq. (4)) by:

$$\Delta\omega(\vec{r}, t) = \gamma(B_0 - \vec{B}(\vec{r}, t))\vec{z} \tag{14}$$

The magnetization computation kernel defines three event functions derived from Eq. (5) which are an application of RF pulse, an application of gradient, and a delay corresponding to the spin magnetization relaxation.

The last functionality offered by the kernel is the RF signal acquisition which corresponds to the signal reception by two orthogonal coils placed in the x, y plane of the magnetization state of the object after a given excitation. The RF signal is a one dimensional discrete com-

plex signal that will fill one line of the k-space volume in respect with the excitation sequence.

One point $s[t]$ of the RF signal is obtained by summation of the local magnetization over the entire virtual object (Eq. (15)). The next point is obtained after an evolution of the local magnetization respecting Eq. (5) with a time step Δt equal to the sampling period of the signal.

$$s[t] = \sum_{\vec{r}} \vec{M}(\vec{r},t)\vec{x} + j\sum_{\vec{r}} \vec{M}(\vec{r},t)\vec{y} \tag{15}$$

2.6. T_2^* effect, spin echo and limited number of spin magnetization vectors

As mentioned in Section 1, MRI simulators based on discrete event Bloch equation encounter the following problems: Simulation of intra-voxel inhomogeneities and simulation of spin echoes [1]. Using multi-isochromats within each object voxel (which is offered within SIMRI through the definition of the object components) is an efficient solution for the 1D case [1]. But it is too complex in terms of spin modeling and requires too much computing time [15] to be used for 2D and 3D image simulation. The other approach recently proposed [21] is linked to gradient application and consequently not simulate spin-echo without gradients. We propose an alternative solution that makes possible simulation of 2D and 3D MR image within reasonable computation time, and thus that functions with only one component per object, i.e., one spin magnetization vector within an object voxel. In this condition, two problems occur.

On the first hand, the free induction decay (FID) signal will follow a T_2 decay and not the T_2^* decay due to the large number of isochromats within a voxel created by the intra-voxel field inhomogeneity. The solution of this problem is to use the intra-voxel field inhomogeneities ΔB_i (mentioned in Section 2.3) user defined in each object voxel. Within the computation kernel, the transverse magnetization of each voxel is weighted by $e^{-\gamma \Delta B_i t}$, where t represents the time elapsed from the first RF pulse. This leads to T_2^* decay of the FID and thus to weighting the gradient echo magnitude by T_2^*, as illustrated in Section 3.1.

On the second hand, one problem is to generate real spin echoes with the correct amplitude without application of a gradient, using a unique magnetization vector per voxel. These echoes correspond to the refocusing of the magnetization due to the application of a 180° pulse after the first 90° pulse. It is addressed by introducing a variable τ which is used in the weighting of the transverse magnetization instead of t. The management of the τ variable is illustrated in Fig. 2. τ is set to 0 at the beginning of an excitation defined by the first RF pulse (Fig. 2A). τ equals t during the excitation and is incremented after each event, except after RF pulse(s) (Fig. 2B) where τ is turned to $-\tau$ as in the case of a 180° RF pulse in a spin-echo (SE) sequence. After a time that equals the pulse interval, τ will be zero (Fig. 2C). This corresponds to the spin re-focusing, and consequently, to an echo. If only one pulse is used like in gradient-echo (GE) sequence, τ evolves like t and no refocusing will appear.

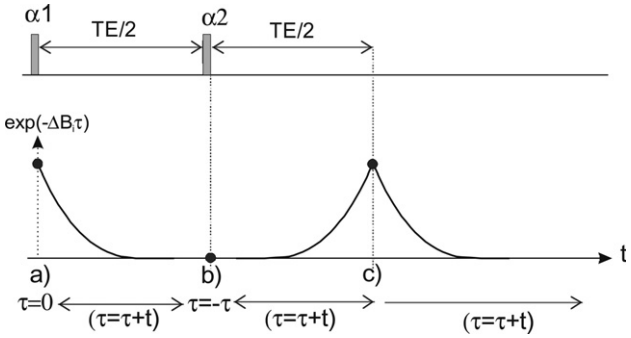

Fig. 2. Time management to simulate the spin refocusing.

This new strategy enables to generate spin-echo train weighted by T_2 and gradient echo train weighted by T_2^* with a very low computation cost, as illustrated in Section 3.1, and to simulate consequently multiple SE or GE imaging weighted by T_2^*.

Lastly, in SE sequence, a too small number of spin magnetization vectors generates a line artifact at the center of the image when repetition time is short because of the transverse magnetization refocusing. We overcome this problem by adding a numerical spoiling after the readout. The spoiling consists in setting the transverse magnetization to zero.

2.7. Noise and filtering

As it is known that the MRI signal is mainly corrupted by thermal noise [26], a white Gaussian noise can be added to the k-space values. The standard deviation of this noise is user defined as illustrated in Fig. 25.

Before MR image reconstruction by the fast Fourier transform, filtering of the k-space is available. We use Hamming filtering of the data to limit the ringing artifact when small size images are simulated, yet any kind of numerical filtering can be used.

3. Simulation results

The *SIMRI* simulator is able to simulate MR images from 1D to 3D in many different ways. In the following, we shall first introduce 1D signals to underline the validity of the proposed T_2^* management method. Then, the RF pulse shaping will be illustrated. We will also give typical 2D simulation results obtained from the McGill

Brain phantom [15] with SE, GE, and true fast imaging with steady-state precession (true FISP) sequences [23,27]. Then, we shall address the simulation of gradient crusher used in slice SE imaging. Lastly, we shall present demonstrative results of the possibility of simulation of images impacted by chemical shift or susceptibility artifact.

3.1. Echo train

Fig. 3 corresponds to the magnitude of the RF signal simulated using a CPMG (Carr–Purcell–Meiboom–Gill) sequence applied on a constant object that is defined by 512 voxels, $\rho = 10$, $T_1 = 250$ ms, and $T_2 = 100$ ms. The intra-voxel field inhomogeneity is constant and is set to 10^{-6} T with a main field of 1 T. As there is no applied gradient, the obtained echoes are spin echoes. Their magnitude follows a T_2 exponential scaling while the echo sides are exponentially scaled by T_2^*, depending on the intra-voxel inhomogeneity value.

Fig. 4 gives the magnitude of the RF signal simulated by applying eight gradient switching after a 90° pulse on the same homogeneous object. Contrary to spin echoes, the echoes are exponentially scaled by T_2^* and the scaling of the echo sides is linked to the gradient value.

The results obtained on echo trains match the theory [23] and validate the proposed approach (Section 2.6) to manage the T_2^* effect with only one spin magnetization vector represented by voxel.

3.2. RF pulse shaping

We simulate the evolution of the magnetization after a $\pi/2$ pulse applied along the x direction of a homogeneous 3D object with $\rho = 100$, $T_1 = 100$ ms, and $T_2 = 100$ ms. We use three different RF pulses of a 2.56 ms duration. The first pulse is a constant rectangular RF pulse. The second one is a sinc-shaped RF pulse with 3 lobes defined by a set of 128 rectangular RF pulses. The third one is a Gaussian shaped RF pulse user-defined by a set of 128 rectangular RF pulses.

The observed transverse magnetization amplitudes are given in Fig. 5. As expected, the constant RF pulse generates side lobes with relatively high amplitudes reaching above 30% of the maximum amplitude. The amplitudes of these lobes are less high when using the sinc-shaped RF pulse (18%). The Gaussian shaped RF pulse gives a signal with the lowest amplitudes lobes

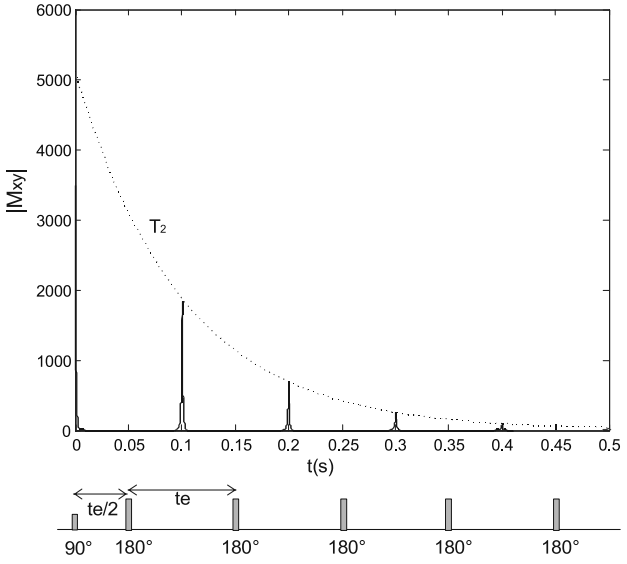

Fig. 3. Simulated signal obtained after a CPMG sequence. It is composed of a train of spin echoes T_2 weighted. The intra-voxel inhomogeneity is set to 10^{-6} T and the main field to 1 T.

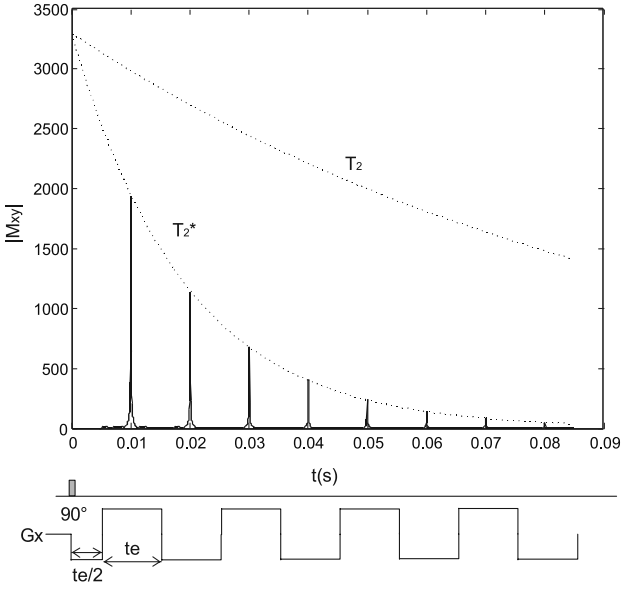

Fig. 4. Simulated signal obtained after a gradient echo pulse sequence. It is composed of a train of T_2^* weighted gradient echoes. The intra-voxel inhomogeneity is set to 10^{-6} T and the main field to 1 T.

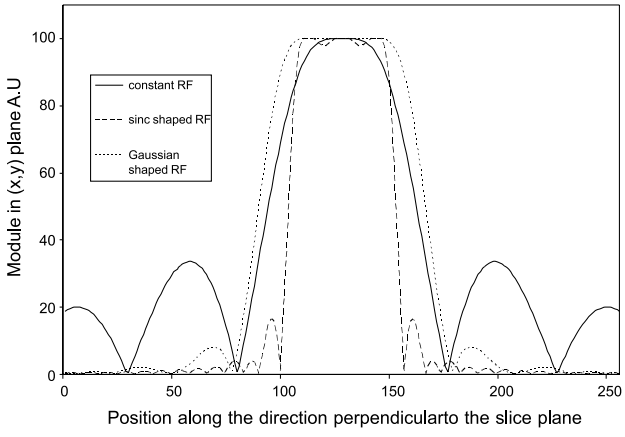

Fig. 5. Signal module evolution in the x, y plane along the axis perpendicular to the slice plane after a $\pi/2$ RF pulse with three different shapes.

(8%) and shows a flat response at the signal center (100–150) compared with the sinc-shaped one where oscillations are observed.

The previous examples show that the use of a set of rectangular RF pulses enables the simulation of any shape of RF pulses.

3.3. Contrast using SE and GE imaging

To illustrate the impact of the sequence parameters on the MRI image contrast, we use a virtual object based on the brain phantom of the McGill brain imaging center [24]. Only the label volume (defining nine different tissues) was used but a variance of the parameter ρ, T_1, and T_2 of each tissue was introduced [15].

3.3.1. SE simulations

The images presented in Fig. 6 are obtained by using a 2D spin-echo sequence with a main field set to 1.5 T and a Hamming filtering before reconstruction. One may observe the right evolution of the image contrast.

Fig. 6A presents a T_1 contrast since the echo time (TE) and the repetition time (TR) are short. On the contrary, Fig. 6B obtained with long TE and TR presents a T_2 contrast. As an example, the cerebro-spinal fluid ($\rho = 100$, $T_1 = 2569$ ms, and $T_2 = 329$ ms at 1.5 T) appears almost black in the T_1 contrasted image (Fig. 6A) while it appears white in the T_2 contrasted image (Fig. 6B).

3.3.2. GE simulations

The images presented in Fig. 7 are obtained by using a 2D GE sequence with a main field set to 1.5 T and a Hamming filtering before reconstruction. One may observe the right evolution of the image contrast with the RF pulse flip angle. With a flip angle of 60° (Fig. 7B), the contrast is T_1 weighted, while using a very low flip angle (Fig. 7A) the proton density weighting is predominant [23].

3.3.3. True-FISP simulations

Fig. 8 illustrates the simulation results that we may obtain when using a true-FISP sequence [27] implemented as illustrated in Fig. 10. With such a steady-state precession sequence, both the transverse and the longitudinal magnetization contribute to the signal, thanks to perfect balance of the imaging gradients. The obtained contrast (Fig. 8A) is function of the ratio T_1/T_2^* and is largely independent of TR which can be very short providing fast acquisition sequence [23]. Also, this sequence is very sensitive to static field inhomogeneities [28,29] as underlined by Fig. 8B. Such artifacts are linked to the default intensity (Fig. 8B vs Fig. 9A), the RF pulse angle and the TR value (Fig. 9).

3.4. 3D simulations

The *SIMRI* simulator includes 3D SE and GE sequences. These sequences include a phase encoding along two directions and a frequency encoding along the third direction during the readout. They provide a 3D *k*-space that is reconstructed using 3D FFT. As the magnetization kernel is entirely designed in 3D and as all the functions that are used to build the sequence (see Section 4.1) are also designed in 3D, 3D simulations do not require specific software development, but induce high computation time (see Table 1).

Fig. 11 gives an example of a 3D MRI image. It was obtained from a 64^3 virtual object after 210 min of simulation on a cluster of 8 Pentium III-1 GHz.

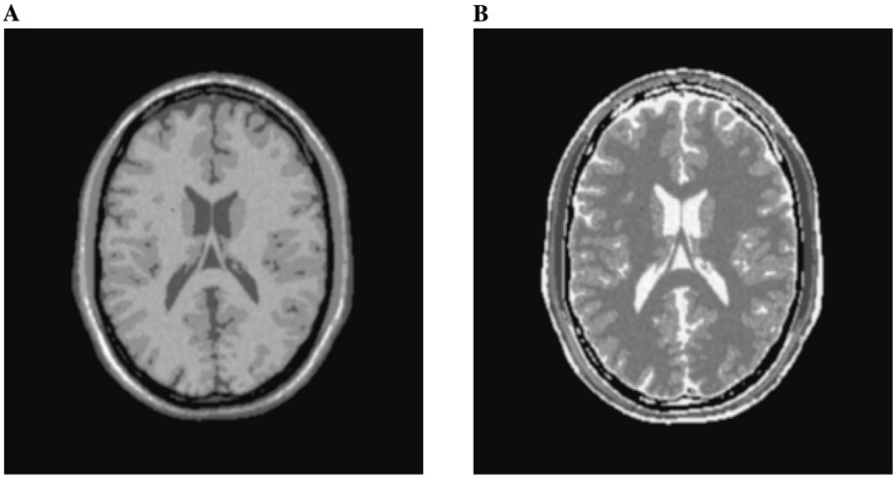

Fig. 6. Contrast variation in spin echo imaging at 1.5 T on a 256×256 brain image. (A) T_1 weighting. (B) T_2 weighting.

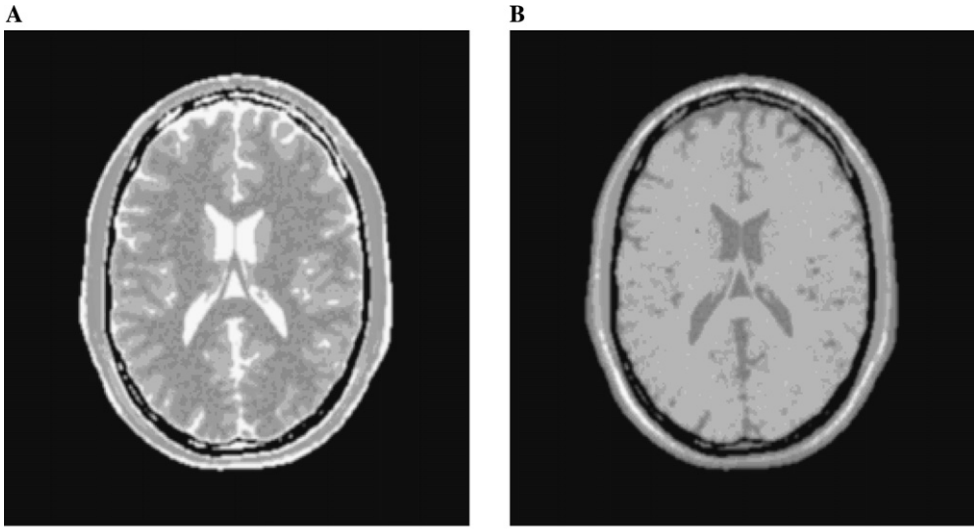

Fig. 7. Impact of the RF flip angle α on the image contrast when using gradient echo imaging at 1.5 T on a 256×256 brain image with TE = 4.25 ms, TR = 25 ms, and a bandwidth BW = 256 kHz.

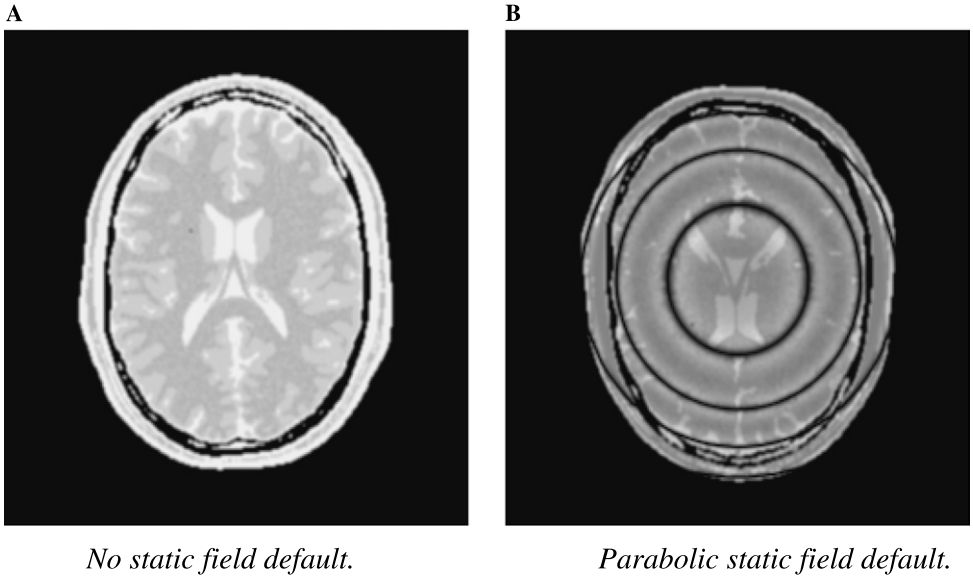

Fig. 8. True FISP simulations with an RF pulse of 20° and 300 μs duration, a readout bandwidth BW = 256 kHz, $B_0 = 1.5$ T and a TR = 4 ms. (A) Image simulated with no static field default. (B) Image simulated with a parabolic static field default with a maximum intensity of 6×10^{-5} T.

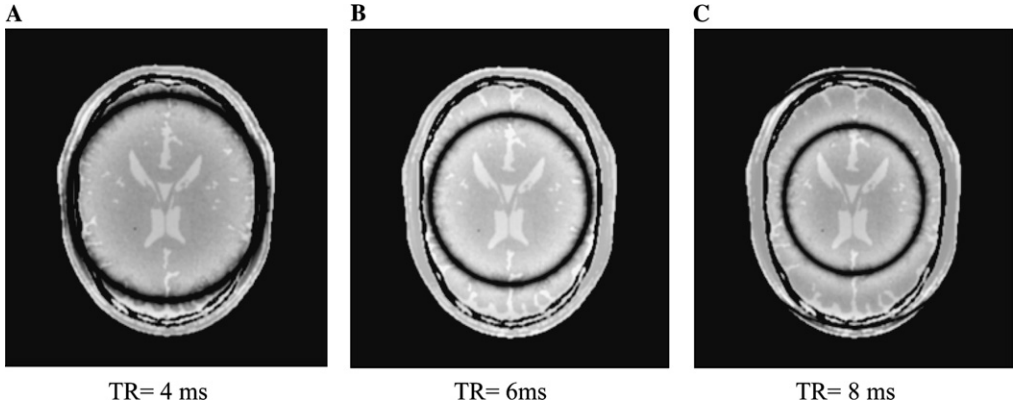

Fig. 9. Repetition time (TR) effect on True FISP acquisitions in presence of a static field inhomogeneity. Images simulated with an RF pulse of 20° and 300 μs duration, a readout bandwidth BW = 256 kHz, $B_0 = 1.5$ T and a parabolic static field default with a maximum intensity of 1×10^{-5} T.

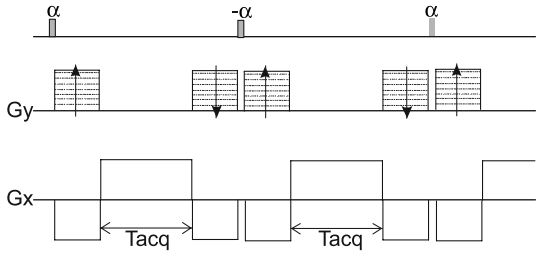

Fig. 10. Two-dimensional true FISP sequence implementation used to obtained images of Figs. 8 and 9.

3.5. Gradient crushing and slice selection

As the π pulse is not perfect in spin-echo sequence, this creates its own FID signal immediately following the pulse [30]. This results in a bright modulated line along the x axis. To overcome the problem, one solution is to use gradient crushing. The slice selection gradient is extended on both sides from the center of the π pulse (Fig. 12). The FID part of the signal is dephased by the gradient lobe which occurs after the π pulse while the spin echo part is unchanged thanks to the symmetry of the gradient around the π pulse.

In MRI simulation, it is necessary to have enough spin magnetization vectors to simulate the gradient spoiling and to avoid unwanted stimulated echoes [20]. Indeed, the discrete summation of the spin magnetization vectors in the presence of a spoiler gradient leads to a residual magnetization reaching a maximum which is function of the spoiling strength.

Fig. 13 presents three simulated images of size 64×64 pixels obtained with TE = 20 ms and TR = 4 s, a readout time of 12.8 ms and the RF pulses are Gaussian shaped defined by 128 rectangular RF pulses. The virtual object is a parallelepiped defined by $T_1 = 100$ ms and $T_2 = 100$ ms. Its size is $200 \times 200 \times 50$ mm^3. It is composed by 64×64 voxels in the x,y plane and 32 or 64 ones in the z direction as discussed below. Note that a spin magnetization vector is associated to each voxel.

First, we use 64 voxels in the direction perpendicular to the slice plane but we turned off the crusher gradients. In this case, a bright modulated line appears as expected (Fig. 13A). When turning on the crusher gradients, the line disappears and the simulated image is free of artefact (Fig. 13B). Then, we decrease the object resolution in the z direction to 32 voxels with the crusher gradients still turned on. Despite the crusher gradients, a bright modulated line appears on the simulated image (Fig. 13C). This is due to improper simulation of crushing when using a too small number of magnetization vectors.

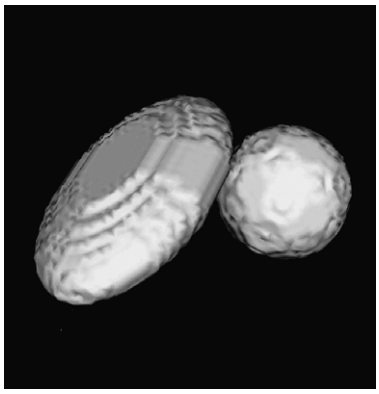

Fig. 11. 3D visualization of a simulated MRI volume ($64 \times 64 \times 64$ voxels) using a T_1 weighted 3D spin echo. The virtual object is composed of an elliptic region ($T_1 = 500$ ms, $T_2 = 90$ ms, and $\rho = 70$) and a spherical region ($T_1 = 350$ ms, $T_2 = 375$ ms, and $\rho = 60$) surrounded by air.

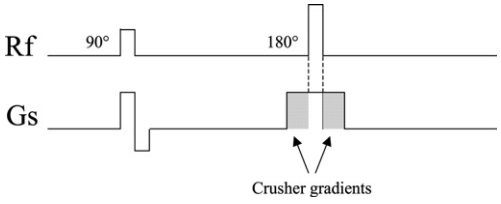

Fig. 12. Gradient crushing position in a spin echo sequence. Diagram of the radio-frequency and of the slice selection gradient Gs.

3.6. Chemical shift artefact

In this section, we shall illustrate some of the possibilities of *SIMRI* to simulate chemical shift artifact thanks to the possible description of an object by many components. We will use two components corresponding to the water proton and the fat proton and the virtual object defined in Fig. 14. Note that *SIMRI* does not limit the number of components.

Figs. 15A and B illustrate the off-resonance phenomena due to the resonance frequency variation (225 Hz at 1.5 T) of the fat and water protons. If the simulator is configured to work on-resonance only, all the RF pulses produce the same flip angle for the two components.

Table 1
2D and 3D MRI simulation computation time using a spin echo sequence

Object size	64^2	128^2	256^2	512^2	1024^2	32^3	64^3	128^3
Image size	64^2	128^2	256^2	512^2	1024^2	32^3	64^3	64^3
Time	3.4 s	43.1 s	12 m	201 m	3277 m	3.5 m	210 m	1626 m

Simulation done on a cluster of 8 PC PIII-1 GHz.

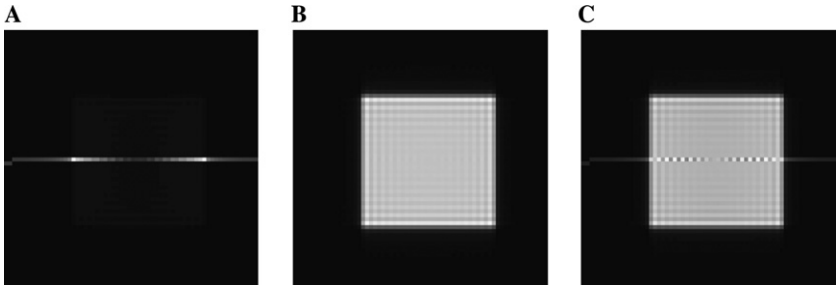

Fig. 13. Examples of slice selection. 64×64 MRI simulated images obtained with 64 object voxels in the z direction without crusher gradients (A) and with crusher gradients (B). With crusher gradients but with only 32 object voxels in the z direction (C).

When allowing off-resonance simulation, only the water protons are on-resonance and the fat protons are off-resonance and thus experience a different flip angle. Consequently, the part of the RF signals coming from the fat proton is frequency shifted. This introduces (Fig. 15B) a modulation of the central line of the image within the fat object, after the FFT reconstruction. The modulation frequency is linked to the frequency shift of the two components and thus to the static field value. In our implementation, the first component gives the reference resonance frequency and thus is always considered on-resonance. The off-resonance simulation is done by adding in Eq. (14) the frequency shift associated with the considered component. Note that this frequency shift is proportional to the local field value defined by Eq. (4).

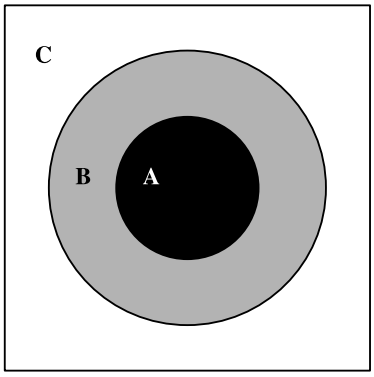

Fig. 14. Virtual object of size 20 cm by 20 cm defined by 256×256 voxels and three regions. Region A is composed of 80% of fat protons ($T_1 = 200$, $T_2 = 750$ at 1.5 T) and 20% of water protons ($T_1 = 3000$, $T_2 = 200$ at 1.5 T). Region B is 100% water protons and region C contains no proton like air.

Fig. 16 illustrates the impact of different parameters on the chemical shift like the readout bandwidth, the static field, or the image size. As expected, the chemical shift artifact decreases as the bandwidth increases.

The comparison of Figs. 15A and 16A shows the impact of the main static field on the shift which increases with the static magnetic field value.

Fig. 17 illustrates the echo time impact on the chemical artifact in gradient-echo imaging. Indeed, if the echoes are not spin echoes, for specific values (given by Eq. (16)) of the frequency shift (Δf) between the considered components and the echo time (TE), the fat signal and the water signal are in phase opposition and as a consequence, the hyper signal part of the image (Fig. 17A) is nullified (Fig. 17B).

$$2\pi \Delta f \, TE = (2k + 1)\pi. \tag{16}$$

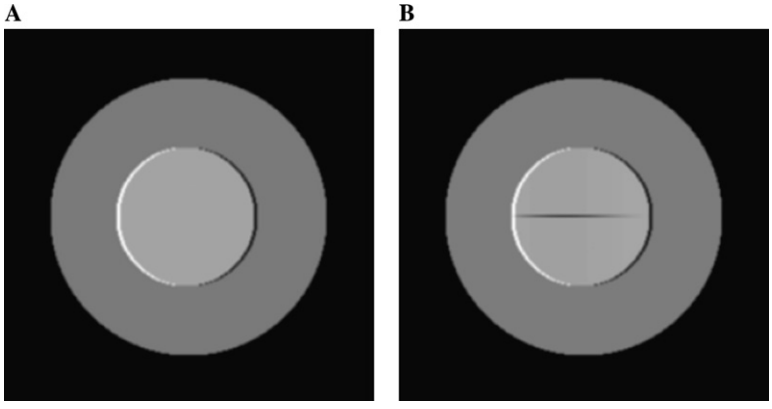

Fig. 15. Simulated images obtained with the same spin echo sequence (TE = 20 ms, TR = 2500 ms, and BW = 25.6 kHz) at $B_0 = 1.5$ T applied on the virtual object presented Fig. 14. Image (A) is obtained by considering that excitation of fat and water protons are on-resonance. Image (B) is obtained by considering that water protons are excited on-resonance while fat protons are excited off-resonance.

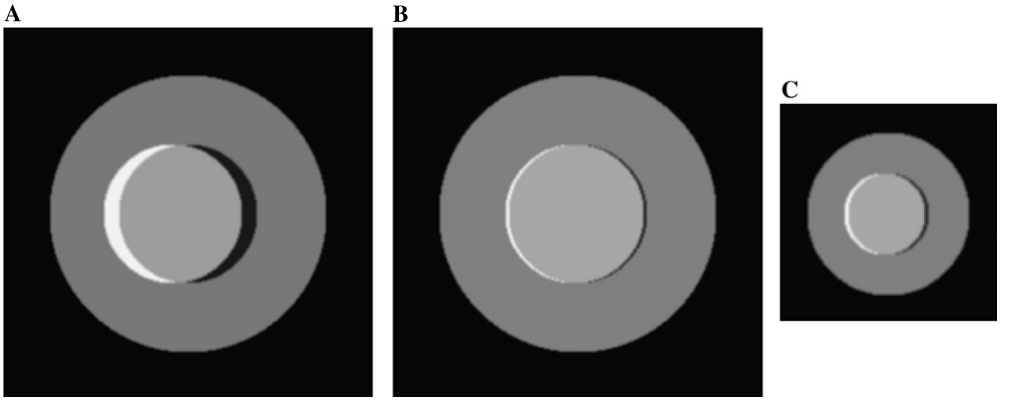

Fig. 16. Impact of the static field, the bandwidth and the image size ($N \times N$) on the chemical shift using a spin echo sequence with TE = 20 ms TR = 2500 ms at $B_0 = 7$ T and the virtual object defined Fig. 14.

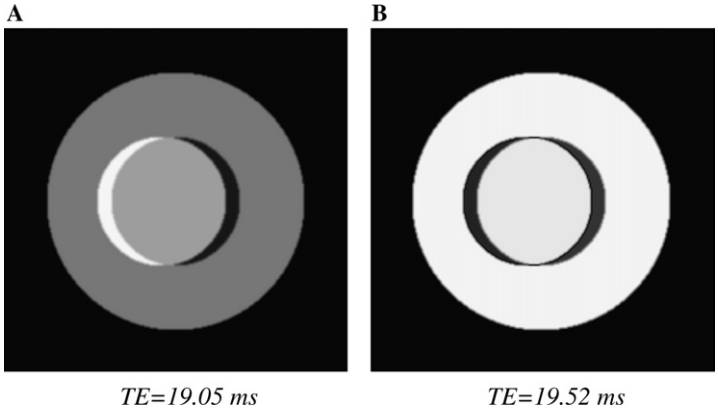

Fig. 17. TE effect on the chemical shift in a gradient echo sequence with $B_0 = 7$ T, a flip angle of 60° and a bandwidth of 25.6 kHz.

3.7. Susceptibility artifact

To illustrate the simulation of the susceptibility artifact, we use a 256^3 virtual object that is a spherical air bubble (diameter: 2.5 cm) within water. The main field inhomogeneities induced by the susceptibility difference between water ($k_i = -9$ ppm) and air ($k_i = 0$ ppm) was precomputed by using a boundary integral method [25]. The field inhomogeneities (namely the ΔB map) are taken into account by *SIMRI*. Into the image they introduce signal loss as well as geometrical and intensity distortions along the readout gradient direction. The susceptibility effects depend [31] on the sequence used, the main field value, the receiver bandwidth and the echo time.

Fig. 18 presents one of the comparisons between real and simulated images that were done to validate the susceptibility effect simulation. The real image (Fig. 18A) was obtained using a physical phantom and a 7 T MRI device. This image and the distortions due to the susceptibility artifact are similar to the one simulated from the virtual object (Fig. 18B). Note that the use of a ΔB map computed from real acquisition (Fig. 18C) produces the correct geometrical distortion in the simulated image but introduces artifacts due to the physical phantom imperfections that are not modeled in the virtual phantom.

Fig. 19 illustrates the sequence impact. With a spin-echo sequence, only geometric and intensity distortions appear on the image. With a gradient-echo sequence, signal losses are added to the distortions [32].

The main static field intensity B_0 impacts the distortions as it can be observed in Fig. 19B and in Fig. 20B simulated, respectively, with $B_0 = 7$ T and $B_0 = 4.7$ T. The higher B_0 is, the more pronounced the distortions are.

In gradient-echo images, the signal losses are only impacted by the echo time TE [33]. They are more important with high TE values, as illustrated in Fig. 20.

Lastly, the receiver bandwidth (BW) also affects the distortions as shown in Fig. 21. As the BW increases, so does the readout gradient. As a consequence, the

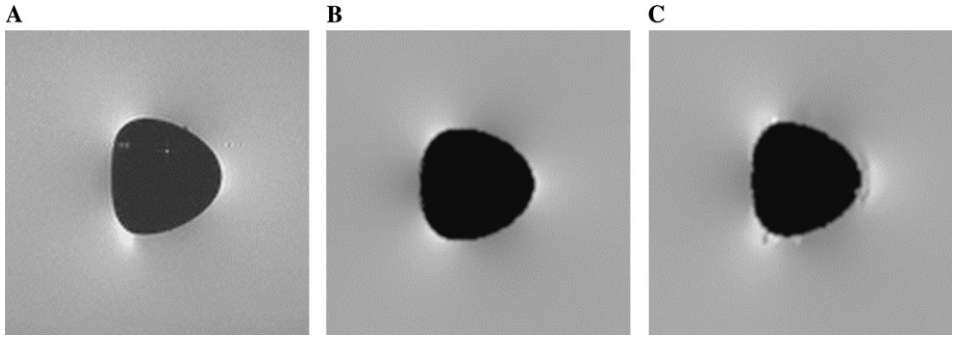

Fig. 18. Comparison of real and simulated images using a spin echo sequence with a bandwidth per pixel of 130 Hz, TE = 24 ms, and TR = 500 ms. (A) Real image obtained on a 7 T MRI device. Simulated images obtained using a virtual object similar to the real one and a ΔB map obtained from the phase unwrapping of a real gradient acquisition (B) or a ΔB map obtained using a boundary integral method [25] and the object geometry knowledge (C).

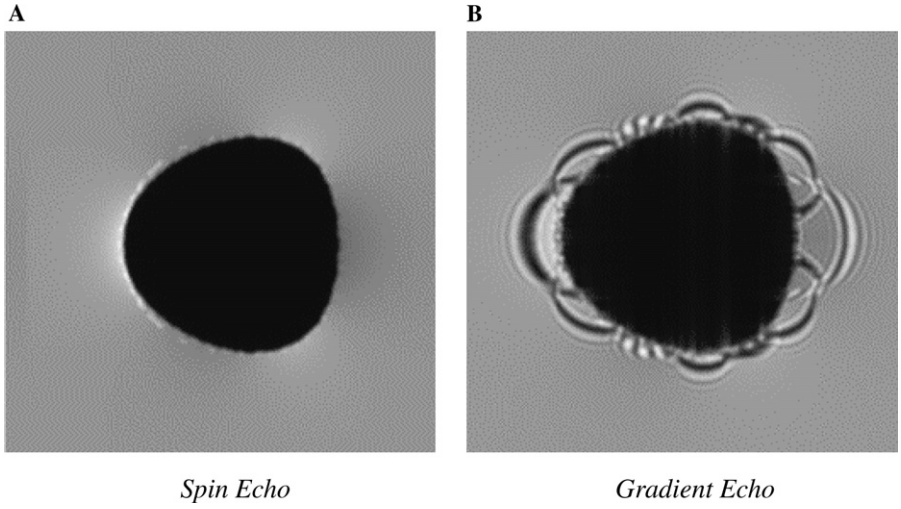

Fig. 19. Illustration of the susceptibility artifact on an air bubble into water with a static field of 7 T. Impact of the sequence type. (A) spin echo sequence (TE = 20 ms, TR = 1000 ms, and BW = 20 kHz). (B) Gradient echo sequence (TE = 20 ms, TR = 1000 ms, BW = 20 kHz, and $\alpha = 90°$). 256×256 simulations.

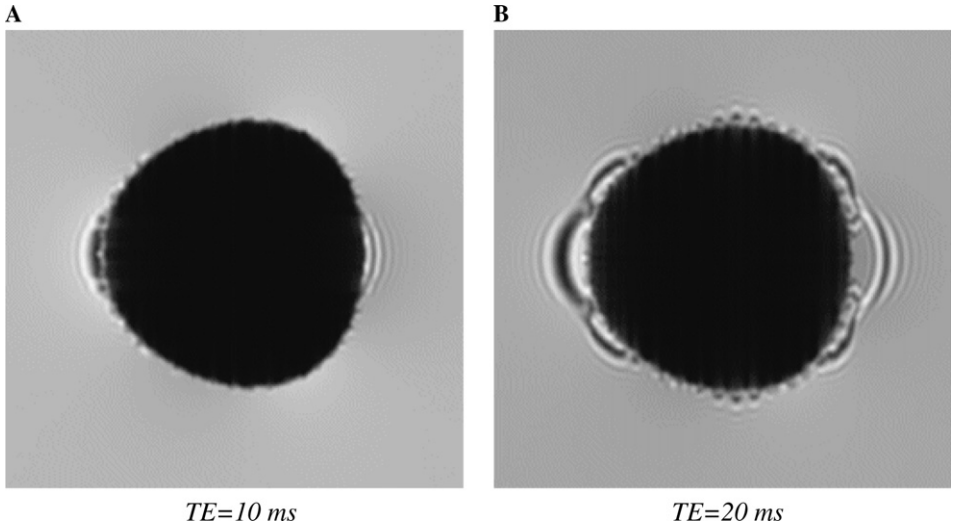

Fig. 20. Illustration of the susceptibility artifact on an air bubble into water with a static field of 4.7 T. Impact of the TE parameter using a gradient echo sequence ($\alpha = 90°$, TR = 1500, and BW = 50 kHz). (A) TE = 10 ms (B) TE = 20 ms. 256×256 simulations.

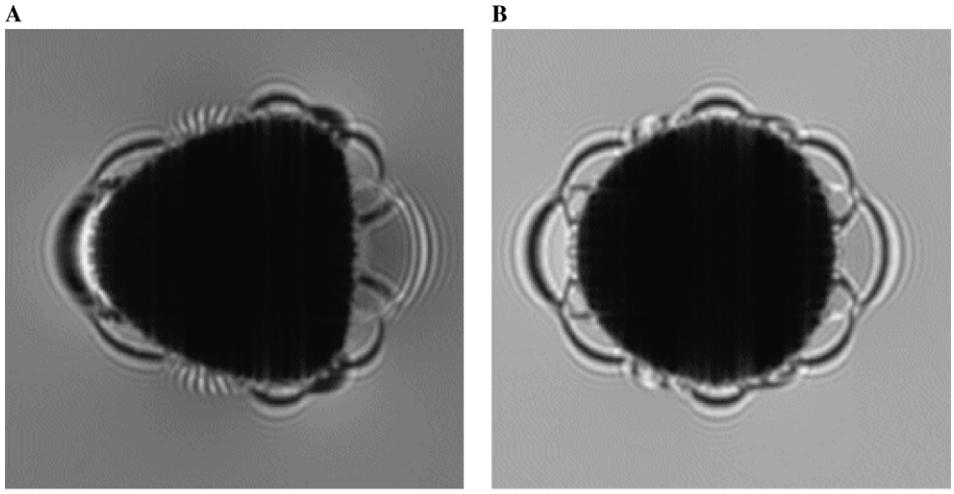

Fig. 21. Illustration of the susceptibility artifact on an air bubble into water with a static field of 7 T. Impact of the bandwidth (BW) parameter using a gradient echo sequence ($\alpha = 90°$ TE = 20 ms, and TR = 1500 ms). (A) BW = 25 kHz. (B) BW = 100 kHz. 256×256 simulations.

distortions decrease. However, the signal losses are still present and carry out the same intensity as they are linked to the TE value only [31].

4. Simulator implementation

The whole code of the *SIMRI* simulator is written in ANSI C language and is divided into different software modules, as shown in Fig. 22. One module concerns the virtual object manipulations and definitions. One module implements MRI sequences. One module deals with image reconstruction. One module is related to the magnetization computation kernel and one module offers several visualization and output functions. Eventually, one module deals with several tests that can be launched with a command line. Note that all these modules work similarly under *Microsoft Windows* and *Linux* operating systems.

The whole simulation package is linked into a dynamic library wrapped for being used with the *Python* scripting language [34]. Such a library was used to develop an interactive portable 1D simulator for pedagogical purpose (see Section 4.2) being close to the one recently developed for NMR spectroscopy [35].

Lastly, the magnetization kernel is parallelized to enable the simulator to run on data grid architecture [36–38] in order to reduce the simulation time significantly.

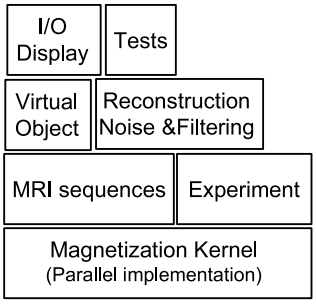

Fig. 22. Overview of the SIMRI simulator module organization.

4.1. Sequence programming and acquisition programming

At the moment, *SIMRI* contains spin-echo, gradient-echo sequences for 1D, 2D, and 3D images as well as their turbo versions. It also contains True-FISP, saturation-recovery, as well as inversion-recovery sequences.

Each sequence is implemented within a C-function (similar to the one given in Fig. 24) that implements the spin-echo sequence (Fig. 23). The excitation acquisition sequence is written in a loop that iteratively calls high level action functions such as *DoGradient*, *DoPulseRect* or *DoAcquisitionX*. This last function requires the position in the *k*-space where the readout signal must be saved. Phase gradient value is simply changed with each cycle. The *SetSpoilingFlag* function triggers the transverse magnetization spoiling after each readout. The *ResetToExperiment* function is called to correctly manage the τ variable in the T_2^* weighting (Section 2.6).

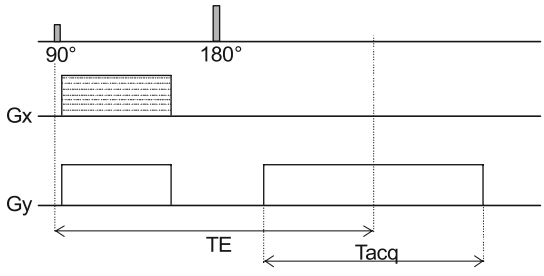

Fig. 23. Spin echo sequence implemented by the function given in Fig. 24.

```
PPPVOLUME_COMPLEX_DOUBLE SeqSpinEcho2D(SEQPARAM *seqparam,EXPERIMENT3D *expr)
{
(…)
 timp=0.3;
 acq_delay = (te/2) - (tacq/2);
 tg = tacq/2.;
 gx = (ntx-1)/tacq/G_kHz_G/fovx;
 gy = (nty-1)/(tg/1000)/G_kHz_G/fovy;
 gz = 0.0;
 npz= 0;

 SetSpoilingFlag(entre,ACTIVE); /* XY Spoiling after acquisition */

 for (npy = 0; npy < expr->nty; npy++)
       {
            ResetToExperiment(expr);
            DoPulseRect(expr,entre, 90.,timp);

            gp = (gy) * (npy - (nty) / 2) / (nty);
            DoGradient(expr,entre,tg,gx,gp,gz);
            DoWaiting(expr,entre,acq_delay);

            DoPulseRect(expr,entre,180.,timp);
            DoWaiting(expr,entre,acq_delay);

            DoAcqFrequenceX( expr,entre, gx, npy, npz, 0, MOINS);

            DoWaiting(expr,entre,tr-te-tacq/2.0);
       }
      NormalizeRFSignal(expr);
 return(GetSignalRFComplexFromExperiment(expr));
}
```

Fig. 24. Example of the C coding of the Fig. 24 2D spin echo sequence.

It is relatively easy for MRI sequence aware people to understand the C code of a sequence. The high level function interface provided by *SIMRI* allows a quick and easy sequence programming having only a minimum knowledge of the C programming language.

Fig. 25 shows one example of a test function that calls a 2D spin-echo sequence. First the virtual object is defined by calling the function *CreateObjectTest2D_CircleEllipse* that creates a geometric object. Other object generation functions are able to read objects saved into files like with anatomical objects. Then the size of the object is given. The intra-voxel inhomogeneity that affects directly the T_2^* is given by calling the *SetDeltaB0Object* function. This particular function sets constant inhomogeneity values. One other function is able to read a 3D map with intra-voxel inhomogeneity values.

Then the experiment structure is defined. It contains the image size, the FOV definition, the readout bandwidth given here through the readout time (*tacq*), the B_0 value, and a flag (*flagres*) that indicates whether the RF pulses are considered always on-resonance or not.

The sequence parameters (TE and TR) are defined before running the sequence. Then the sequence is executed by calling the *RunSequence* function with the chosen sequence named *SE2D*, the defined object with the defined sequence and experiment parameters. Note that *RunSequence* iterates the MRI sequence on all the components that can possibly define the virtual object, and adds their contributions automatically.

The *RunSequence* function returns the *k*-space (*volrf*). The *AddGaussianNoiseToRFVolume* function adds noise to the *k*-space that can be filtered by calling the *VolRFFiltering function*. Note that in the example, the noise standard deviation (set to 0.001) is not linked to any acquisition parameter explicitly. It is up to the user to implement such links in a few lines. Last, in this example, we only get the module of the reconstructed image that can be saved and visualized.

This example show how high potentialities of the *SIMRI* simulator are in simulating MR images throughout the relatively simple high level C functions call.

4.2. 1D interactive simulation

The *SIMRI* simulator also proposes a highly interactive interface for pedagogical and understanding purpose based on 1D simulation.

Fig. 26 presents the main window of the interface. The upper left part of the window presents the ρ, T_1, and T_2 profiles of the 1D virtual object. In this one example, the object is composed of four different homogeneous parts. This profile can be user defined interactively. The user may define a main field inhomogeneity profile associated with the object. The object definition

```
void TestSequence(int objsize,int imasize,int visu,
                  double tacq,double TE,double TR,double b0, double db0,
                  int flagres,int filter,char * fileout)
 {
 int x,y,z;
 int ntx, nty, ntz;          /* RF volume size */
 double fovx,fovy,fovz;      /* Fov in meter */
 OBJET3D *objet;
 EXPERIMENT3D *expr;
 SEQPARAM seqparam;
 (…)

 /* Object */
 x=objsize; y=x; z=1;
 objet=CreateObjectTest2D_CircleEllipse(x,y);
 SetSizeObject(objet,(float)0.2,(float)0.2,(float)0.002);
 SetDeltaB0Object(objet,db0);

 /* Experiment */
 expr=AllocExperiment();
 ntx=imasize; nty=ntx; ntz=z;
 fovx=0.20; fovy=0.20; fovz=0.0020;
 SetFovExperiment(expr,fovx,fovy,fovz,0.0,0.0,0.0);
 SetAcqExperiment(expr,ntx,nty,ntz,tacq*1e-3);
 SetResonanceExperiment(expr,flagres);
 SetB0Experiment(expr,b0);

 /* Sequence */
 SetSeqParamTE(&seqparam,TE);
 SetSeqParamTR(&seqparam,TR);
 volrf = RunSequence("SE2D",&seqparam,objet,expr);
 FreeObjet(objet);
 AddGaussianNoiseToRFVolume(volrf,0.001);
 if (filter==YES) VolRFFiltering(volrf,HAMMING);
 volrecmod = RecVolIFFTModuleFromVol(volrf);

 /* Output Result */
 if (visu==YES) DisplayVolXY((PPPVOLUME)volrecmod,0,"Recvol2D");
 WriteVolRF(volrf);
 WriteVolRecUchar(volrecmod,fileout);
 IdVolFree(volrecmod);IdVolFree(volrf);
}
```

Fig. 25. Example of the C coding of a full MRI simulation.

may be saved on disk and then be reloaded. Note that an object may be defined by up to two components corresponding to the water and fat protons.

The bottom part of the window deals with the sequence type and parameters that can be modified interactively, impacting the 1D MRI signal. The signal is displayed in the upper right part of the window. User may choose to display the RF signal through its module, phase, real, and imaginary part. The reconstructed signal may be displayed as a signal as well as a grey level line, as it may appear in a complete 2D or 3D acquisition. In the example given in Fig. 26, the image line is being displayed together with the RF signal magnitude and the reconstructed signal.

From the *View* menu in the main window, the user may call a second type of interface that we call the "SpinPlayer," which is illustrated in Fig. 27. The main function of the *SpinPlayer* is to offer a 3D visualization of the object spin magnetization vectors within the rotating frame during one sequence. Such visualization is presented in Fig. 27C with four spin magnetization vectors represented by arrows. The user may configure (Fig. 27B) the number of spin magnetization vectors he wishes to view, as well as their characteristics (ρ, T_1, and T_2). He can also save or load different vector sets. The user may design a sequence by chaining events as RF pulse, gradient and precession (Fig. 27A). User sequence definition may be saved and/or loaded. Once a sequence and a spin magnetization vector set are defined, the user may choose the display speed and the trace length of the spin vectors and then he may play the sequence. During the play, the user may observe vector motions (Fig. 27C) as well as RF signals (that would be acquired by two coils placed on the x and y axis) as well as the magnitude of the combined complex signals (Fig. 27D). Note that the user may interact (zooming,

Fig. 26. Overview of the general interface.

rotation, and translation) with the 3D spin vector visualization window while playing.

4.3. Distributed implementation

In 1D, the *SIMRI* simulator is interactive and it offers real-time simulation on a simple PC. Yet, it is known that such simulation based on the Bloch equation solving at each object point is time consuming [22]. It is also known that distributed or parallel implementation of such type of simulations was found efficient [4]. As an example, the simulation of a 128×128 image takes less than one minute on a Pentium IV-2 GHz PC. Yet, multiplying by two the dimension of the image that must be simulated multiplies by 16 the computation time in 2D and by 64 in 3D [22]. To allow 2D and 3D high-resolution simulations within a reasonable amount of time, we parallelize the magnetization kernel of the simulator [22], in order to distribute the computation task through large clusters of computers, i.e., data grid [37] as such a technology will offer virtually unlimited computing power. The gridification of the *SIMRI* simulator was part of the IST European Data-Grid project [36] and of the French Ministry for Research ACI-GRID project [39].

The parallelization of the magnetization kernel was done using the MPI [40] version of GLOBUS [41]. The MPI standard is widely available with free implementation. Such implementation enables the simulator to run on any massively parallel machine, to run on any workstation cluster that runs MPI, and to run on single PC. The parallelization was designed to be transparent at sequence development level and thus only concerns the modules dedicated to the Bloch equation solving.

Because all the spin magnetization vectors are independent (Eq. (5)) and because the signal acquisition process is linear (Eq. (15)), a parallelization scheme of "divide & conquer" type (Fig. 28) was implemented. This consists in distributing the magnetization computation of a subset of spin magnetization vectors. This subset may be fixed to a given size or adapted to the number of active computation nodes.

All the computation nodes carry the MRI sequence and all receive a part of the virtual object from the master node. They compute the magnetization evolution of the corresponding spin magnetization vector subset. At the end of each acquisition step, the master node collects and adds all the RF signal contributions and stores the RF signal in the k-space. At the end of the MRI sequence, the master node applies the reconstruction algorithm to generate the MRI simulated image.

When using homogeneous grid, the virtual object portion distributed to the nodes has a maximal size that

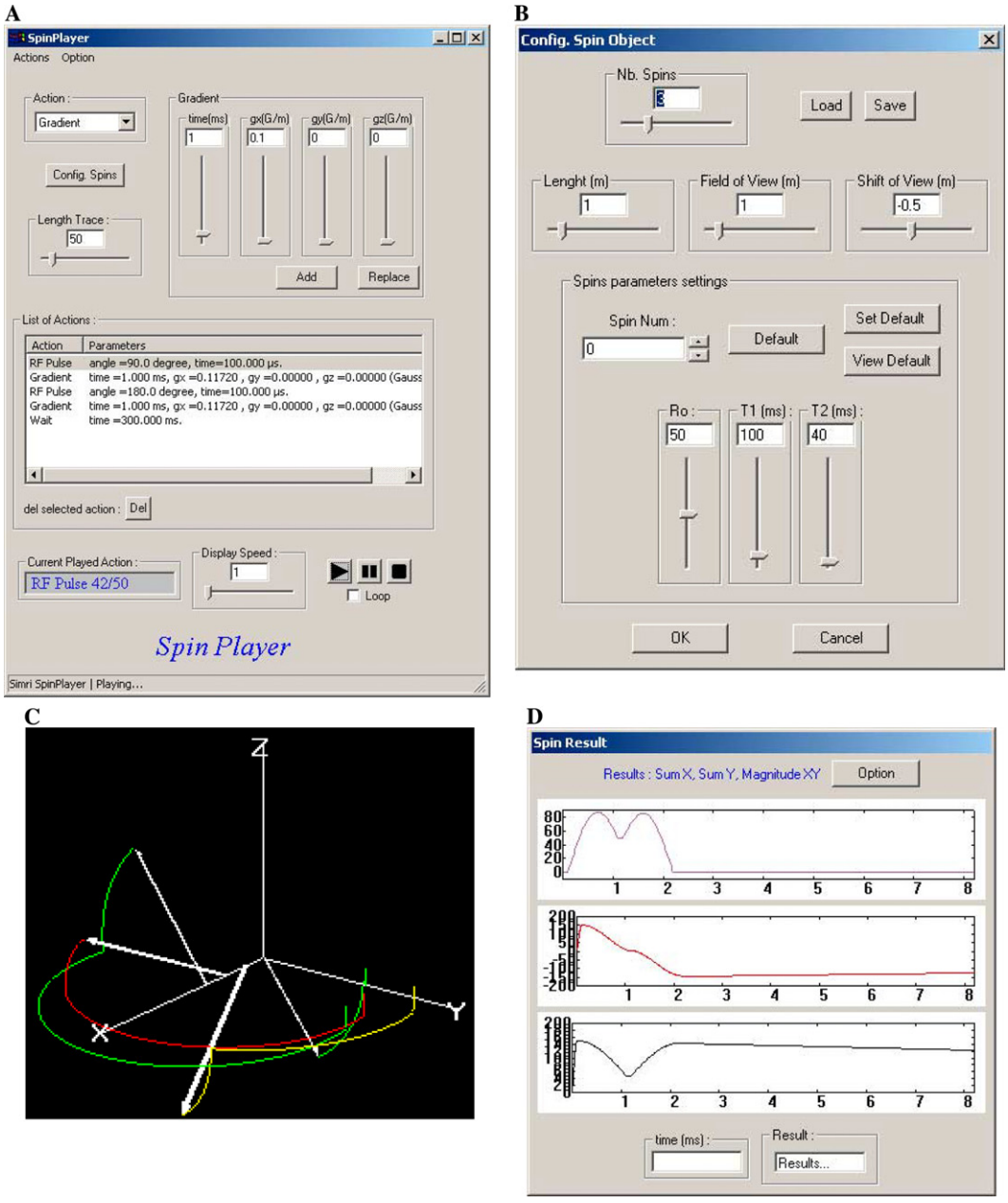

Fig. 27. Illustration of the "SpinPlayer" interface.

is equal to the object size divided by the number of nodes. Only one distribution is done at the process beginning, which limits the communication between the master node and the computation nodes. When using an heterogeneous grid, the distributed object portion is reduced to avoid being handicapped by the slowest node. In that case, the lowest node receives one portion of the object to process, and the fastest nodes receive many.

For different object and image sizes, Table 1 gives computation time values obtained using a small grid based on a PC cluster of 8 Pentium III-1 GHz. Other results given in [22] show that the time gain is linear in re-

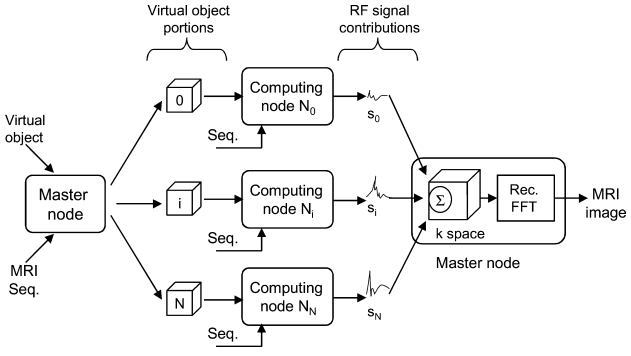

Fig. 28. Data and Process distribution to the grid nodes: a "divide & conquer" scheme.

spect with the number of computation nodes. Those simulation results obtained show that, with a small cluster, MRI simulation of high resolution (1024^2) 2D images is possible within three days. Concerning 3D images, it is not realistic to simulate on such a small set of processors over 64^3 cubic MRI images. Nevertheless, it is possible to simulate 3D multi-slice images (16 slices of 512×512 pixels) within a week. The simulation of high resolution 3D images should be tractable on full scale grids as the ones still under development [37].

5. Conclusion

This paper presented an overview of the *SIMRI* simulation project. This MRI simulation program based on the Bloch equation enables the simulation of 1D, 2D, and 3D images. It includes the simulation of the T_2^* effect at low cost. It takes into account the main static field value and allows the simulation of images impacted by several types of artifacts, including the chemical shift and the inhomogeneities of the static field as those induced by variation of object susceptibility. The simulator is implemented in C language and allows a direct sequence programming by simple high level C function calls strongly evolutionary. The magnetization kernel based on the Bloch equation is implemented in parallelized way that enables the run of simulation on PC grid architecture in order to simulate large images. Furthermore, the same kernel is used to build an interactive simulator for pedagogical purpose illustrating the spin motion as well as the MRI contrast.

The high modularity of the simulation implementation easily allows one to add modules concerning the RF inhomogeneity, the coils receiving properties, the gradient non-linearity. We believe that by integrating in the virtual object design more a priori knowledge such as the statistic properties of the physical parameters and their dependence to the main static field, and by enhancing the noise model that impacts the *k*-space, this simulator will be able to merge the simulation solutions based on cluster [11] as well as on *k*-space modeling [12], to simulate the high precision MRI images that are compulsory for post-processing evaluation. Further work is in prospect concerning the simulation of object with time varying characteristics so as to study perfusion/diffusion modeling and imaging. The susceptibility effect simulation also provides an efficient tool to study paramagnetic contrast agent imaging [15].

For the moment, *SIMRI* is used to evaluate susceptibility artifact correction algorithm [42,43] and it belongs to the core of a new correction approach under development. *SIMRI* also is considered to evaluate and to prescale MRI sequences on a 7 T imager. The *SIMRI* 1D interface is used for practical sessions in Master Courses.

Lastly, we think about transforming the *SIMRI* project into a GPL (Gnu public license) software project in order to allow different researcher communities to take the benefit of it and to make it efficiently evolved.

Acknowledgments

This work is in the scope of the scientific topics of the PRC-GdR ISIS research group of the French National Center for Scientific Research (CNRS). This work is partly supported by the IST European Data-Grid Project [36] and by the French Ministry for Research ACI-GRID project [39]. This work was also funded by the INSA Lyon. The *SIMRI* project was initiated thanks to the work done by G. Soufflet on the initial version of the 1D MRI simulator of J. Bittoun [17]. We thank S. Balac (MAPLY, UMR CNRS #5585) for his contribution to the susceptibility artifact simulation. Many thanks to Y. Zaim-Wadghiri (Skirball Institute of Biomolecular Medicine, NYU Medical Center) for his collaboration on the susceptibility artifact. Many thanks also to F. Bellet and to J. Montagnat (CREATIS, UMR CNRS #5515, U 630 Inserm) for their help in the *SIMRI* parallelization and grid implementation and to G. Bonnilo and to L. Alexandre for their work on the 1D interface. Special thanks are dedicated to M. Blanchet for the English reviewer work.

References

[1] P. Shkarin, R.G.S. Spencer, Direct simulation of spin echoes by summation of isochromats, Concepts in Magnetic Resonance 8 (1996) 253–268.
[2] G. Torheim, P.A. Rinck, R.A. Jones, J. Kvaerness, A simulator for teaching MR image contrast behavior, MAGMA 2 (1994) 515–522.
[3] D. Rundle, S. Kishore, S. Seshadri, F. Wehrli, Magnetic resonance imaging simulator: A teaching tool for radiology, Journal of Digital Imaging 3 (1990) 226–229.
[4] A.R. Brenner, J. Kürsch, T.G. Noll, Distributed large-scale simulation of magnetic resonance imaging, Magnetic Resonance Materials in Biology, Physics, and Medicine 5 (1997) 129–138.
[5] M.B.E. Olsson, R. Wirestam, B.R.R. Persson, A computer-simulation program for Mr-imaging—application to Rf and static magnetic-field imperfections, Magnetic Resonance in Medicine 34 (1995) 612–617.
[6] R.K.-S. Kwan, A.C. Evans, G.B. Pike, An extensible MRI simulator for post-processing evaluation, in: International Conference on Visualization in Biomedical Computing, VBC'96, 1996, pp. 135–140.
[7] S.J. Riederer, S.A. Suddarth, S.A. Bobman, J.N. Lee, H.Z. Wang, J.R. MacFall, Automated MR image synthesis: feasibility studies, Radiology 153 (1984) 203–206.
[8] D.A. Ortendahl, N. Hylton, L. Kaufman, J.C. Watts, L.E. Crooks, C.M. Mills, D.D. Stark, Analytical tools for magnetic resonance imaging, Radiology 153 (1984) 479–488.
[9] S.A. Bobman, S.J. Rieder, J.N. Lee, S.A. Suddarth, H.Z. Wang, B.P. Drayer, J.R. MacFall, Cerebral magnetic resonance image synthesis, AJNR 6 (1984) 265–269.

[10] S.A. Bobman, S.J. Riederer, J.N. Lee, S.A. Suddarth, H.Z. Wang, J.R. MacFall, Synthesized MR images: comparison with acquired images, Radiology 155 (1985) 731–738.
[11] A. Simmons, S.R. Arridge, G.J. Barker, S.C.R. Williams, Simulation of MRI cluster plots and application to neurological segmentation, Magnetic Resonance Imaging 14 (1996) 73–92.
[12] J.S. Petersson, J.-O. Christoffersson, K. Golman, MRI simulation using the k-space formalism, Magnetic Resonance Imaging 11 (1993) 568–577.
[13] W.R. Crum, E. Berry, J.P. Ridgway, U.M. Sivananthan, L.-B. Tan, M.A. Smith, Simulation of two-dimensional tagged MRI, Journal of Magnetic Resonance Imaging 7 (1997) 416–424.
[14] W.R. Crum, E. Berry, J.P. Ridgway, U.M. Sivananthan, L.-B. Tan, M.A. Smith, Frequency-domain simulation of MR tagging, Journal of Magnetic Resonance Imaging 8 (1998) 1040–1050.
[15] R.K.S. Kwan, A.C. Evans, G.B. Pike, MRI simulation-based evaluation of image-processing and classification methods, IEEE Transaction on Medical Imaging 18 (1999) 1085–1097.
[16] F. Bloch, Nuclear induction, Physical Review 70 (1946) 460–474.
[17] J. Bittoun, J. Taquin, M. Sauzade, A computer algorithm for the simulation of any nuclear magnetic resonance (NMR) imaging method, Magnetic Resonance Imaging 3 (1984) 363–376.
[18] P. Shkarin, R.G.S. Spencer, Time domain simulation of Fourier imaging by summation of isochromats, International Journal of Imaging Systems and Technology 8 (1997) 419–426.
[19] R.M. Summers, L. Axel, S. Israel, A computer simulation of nuclear magnetic resonance imaging, Magnetic Resonance in Medicine 3 (1986) 363–376.
[20] I. Marshall, Simulation of in-plane flow imaging, Concepts in Magnetic Resonance 11 (1999) 379–392.
[21] D.A. Yoder, E. Changchien, C.B. Paschal, J.M. Fitzpatrick, MRI simulator with static field inhomogeneity, in: SPIE Medical Imaging, vol. 4684, 2002, pp. 592–603.
[22] H. Benoit-Cattin, F. Bellet, J. Montagnat, C. Odet, Magnetic resonance imaging (MRI) simulation on a grid computing architecture, in: IEEE CGIGRID'03- BIOGRID'03, Tokyo, 2003, pp. 582–587.
[23] Z.P. Liang, P.C. Lauterbur, Principles of Magnetic Resonance Imaging. A Signal Processing Perspective, IEEE Press, New York, 2000.
[24] D.L. Collins, A.P. Zijdenbos, V. Kollokian, J.G. Sled, N.J. Kabani, C.J. Holmes, A.C. Evans, Design and construction of a realistic digital brain phantom, IEEE Transaction on Medical Imaging 17 (1998) 463–468.
[25] S. Balac, H. Benoit-Cattin, T. Lamotte, C. Odet, Analytic solution to boundary integral computation of susceptibility induced magnetic field inhomogeneities, Mathematical and Computer Modelling 39 (2004) 437–455.
[26] W.A. Edelstein, G.H. Glover, C. Hardy, J.R.W. Redington, The intrinsic signal to noise ratio in NMR imaging, Magnetic Resonance Imaging 3 (1986) 604–618.
[27] A. Oppelt, R. Graumann, H. Barfuß, H. Fischer, W. Hartl, W. Schajor, FISP: a new fast MRI sequence, Electromedica 54 (1986) 15–18.
[28] L. Darrasse, L. Mao, H. Saint-Jalmes, Steady-state management in fast low-angle imaging, in: SMRM Annual Meeting, Montreal, 1986, pp. 944–945.
[29] L. Darrasse, L. Mao, H. Saint-Jalmes, Fast field mapping by NMR interferometry, in: Topical Conference on Fast MRI Techniques, Cleveland, 1987.
[30] E.M. Haacke, R.W. Brown, M.R. Thompson, R. Venkatesan, Imperfect pi-pulses, in: Their Effects on Spin Echo Images and Reduction of the Resulting Artifacts, Magnetic Resonance Imaging: Physical Principles and Sequence Design, Wiley, 1999, pp. 809–811.
[31] A.M. Abduljalil, P.M. Robitaille, Macroscopic susceptibility in ultra high field MRI, Journal of Computer Assisted Tomography 23 (1999) 832–841.
[32] J.R. Reichenbach, R. Venkatesan, D.A. Yablonskiy, M.R. Thompson, S. Lai, E.M. Haacke, Theory and application of stativ field inhomogeneity effects in gradient-echo imaging, Journal of Magnetic Resonance Imaging 7 (1997) 266–279.
[33] S. Posse, W.P. Aue, Susceptibility artifacts in spin-echo and gradient-echo imaging, Journal of Magnetic Resonance 88 (1990) 473–492.
[34] D.M. Beazley, Python, Essential Reference, second ed., New Riders, 2001.
[35] P.J. Letourneau, PJNMR: a platform-independent graphical simulation tool for NMR spectroscopy, Journal of Magnetic Resonance 161 (2003) 154–167.
[36] Datagrid, European DataGrid project. Available from: <http://eu-datagrid.web.cern.ch/eu-datagrid/>.
[37] I. Foster, C. Kesselman, S. Tuecke, The anatomy of the grid: enabling scalable virtual organisations, International Journal of Supercomputer Applications 15 (2001).
[38] J. Montagnat, V. Breton, I.E. Magnin, Using grid technologies to face medical image analysis challenges, in: IEEE CCGrid'03, Tokyo, 2003, pp. 588–593.
[39] MEDIGRID, ACI-GRID project, French Research Ministry. Available from: <http://www.creatis.insa-lyon.fr/medigrid>.
[40] MPITCH. Available from: <http://www-unix.mcs.anl.gov/mpi/mpich/>.
[41] Globus. Available from: <http://www.globus.org/gt2.2/>.
[42] B. Belaroussi, Y. Zaim-Wadghiri, H. Benoit-Cattin, C. Odet, D.H. Turnbull, Distortion correction for susceptibility-induced artifacts in spin echo MR images: simulation study at 1.5 T and 7 T, in: ISMRM'04, Tokyo, 2004, p. 2168.
[43] B. Belaroussi, H. Benoit-Cattin, F. Loiseaux, C. Odet, Comparison of spin echo distortion correction methods based on field map, in: ESMRM'04, Copenhagen, 2004, p. 541.